






# Synchrotron Intensity and Polarization Gradients: Tools to Obtain the Magnetization Level in a Turbulent Medium

Lorena Carmo<sup>1,2</sup> , Diego F. González-Casanova<sup>2</sup> , Diego Falceta-Gonçalves<sup>1,3</sup> , Alex Lazarian<sup>2</sup>, Francisco Jablonski<sup>1</sup>, Jian-Fu Zhang<sup>2,4</sup>, Ivan Ferreira<sup>5</sup>, Manuel Castro<sup>1</sup>, and Bo Yang<sup>2</sup>

<sup>1</sup> Divisão de Astrofísica, Instituto Nacional de Pesquisas Espaciais–INPE, Av. dos Astronautas 1758, S. J. Campos, SP 12227-010, Brazil; [lorena.jesus@inpe.br](mailto:lorena.jesus@inpe.br), [lorenadocarmojesus@gmail.com](mailto:lorenadocarmojesus@gmail.com)

<sup>2</sup> Astronomy Department, University of Wisconsin, Madison, WI 53711, USA

<sup>3</sup> Escola de Artes, Ciências e Humanidades, Universidade de São Paulo, Rua Arlindo Bettio 1000, São Paulo, SP, 03828-000, Brazil

<sup>4</sup> Department of Physics, Xiangtan University, Xiangtan, Hunan 411105, People’s Republic of China

<sup>5</sup> Instituto de Física, Universidade de Brasília, Brasília, 70910-900, Brazil

Received 2019 October 2; revised 2020 October 6; accepted 2020 October 12; published 2020 December 21

## Abstract

Synchrotron intensity and polarization gradients (SIG and SPG), proposed by Lazarian et al. and Lazarian & Yuen, present a new way to recover the mean magnetic field direction in the plane of the sky. To measure the magnetization level, Lazarian et al. suggested that the methods used in the context of the “Velocity Gradient Technique” could also be used on the SIG and SPG contexts. In this work we test the two proposed methods, named “top-base” and the circular standard deviation, “S,” to obtain the level of magnetization from synchrotron emission. In order to test the methods, we generate synthetic observations from magnetohydrodynamic computer simulations, with Alfvénic Mach numbers,  $M_A \in [0.2, 1.7]$ . Using a Bayesian analysis we find that the circular standard deviations for the SIG and SPG methods are able to recover the magnetization for cases with signal-to-noise ratio  $\gtrsim 5$ . We found that for weak Faraday depolarization and different angles between the magnetic field direction and the line of sight the magnetization level can still be estimated.

*Unified Astronomy Thesaurus concepts:* [Magnetohydrodynamics \(1964\)](#); [Interstellar synchrotron emission \(856\)](#); [Interstellar medium \(847\)](#); [Interstellar plasma \(851\)](#)

## 1. Introduction

Magnetic fields and turbulence are ubiquitous in the interstellar medium (ISM), being present in the Milky Way and other galaxies (e.g., Zweibel & Heiles 1997; Stanimirovic et al. 2000; Chepurnov & Lazarian 2010; Falceta-Gonçalves et al. 2014; Planck Collaboration et al. 2016). In addition, turbulence modifies the dynamics of the magnetic field, which induces different plasma mechanisms, such as reconnection and the diffusion of the field lines (Lazarian & Vishniac 1999; Lazarian 2005). The combined effect of both phenomena plays a critical role in several astrophysical processes regarding propagation and acceleration of cosmic rays, galaxy dynamics, star formation, transition phases of the ISM, to name just a few (e.g., Ostriker 2003; Ballesteros-Paredes et al. 2007; McKee & Ostriker 2007; Brandenburg et al. 2012; Beresnyak & Lazarian 2019). Therefore, the understanding of the ISM depends on the understanding of the intrinsic properties of magnetohydrodynamic (MHD) turbulence (see Elmegreen & Scalo 2004; Brandenburg & Lazarian 2013).

Observationally, the main techniques used to study MHD turbulence are based on column density, line velocity profiles, and Faraday rotation measures to obtain the fluctuations power spectrum (Armstrong et al. 1995; Haverkorn et al. 2008; Chepurnov & Lazarian 2010; Chepurnov et al. 2015; Mao et al. 2015). However, despite the power spectrum of these quantities being a useful tool for obtaining information about energy transport over different scales, it does not provide a full description of turbulence properties. This can be understood by projection effects on the plane of the sky and the lack of phase information, an important quantity for a complete description in the Fourier space (Burkhart et al. 2009).

Different statistical tools can provide information to understand the properties of the turbulent medium such as sonic and Alfvénic Mach numbers ( $M_S$  and  $M_A$ , respectively). Such techniques have been developed using numerical simulations to understand the properties of the interstellar MHD theory (Burkhart & Lazarian 2011). They include the Delta Variance Analysis applied in simulated molecular clouds (Stutzki et al. 1998; Ossenkopf et al. 2008), Principal Component Analysis (PCA) applied to spectral line imaging studies (Heyer & Peter Schloerb 1997; Heyer et al. 2008; Correia et al. 2016; Ensor et al. 2017), Probability Density Functions (PDF) including the Tsallis Variant of the gas density and the magnetic field structure (Federrath et al. 2008; Burkhart et al. 2012; González-Casanova et al. 2018), PDF of filamentary structures of HI column density (Makarenko et al. 2015), density bispectrum analysis (Burkhart et al. 2009), topological techniques (such as Genus; Chepurnov et al. 2008; Kowal et al. 2009), the Betti number calculation of the gas density fluctuations (Makarenko et al. 2018), the Velocity Channel Analysis (VCA) and the Velocity Coordinate Spectrum (VCS) techniques for optically thick spectral lines in different absorbing media contexts (Lazarian & Pogosyan 2004, 2006, 2012), among others. The use of numerical simulations is important not only to physically understand the complex structures and properties of the different ISM phases, but also to propose tools that can be used in the observations of these environments (e.g., von Weizsäcker 1951; Scheffler 1967; Baker 1973; O’Dell & Castaneda 1987; Oey & Clarke 1997; Esquivel et al. 2003; Falgarone et al. 2005; Hily-Blant & Falgarone 2009; Chepurnov & Lazarian 2010; Krumholz & Burkhart 2016).

In addition, one can also directly study the properties of MHD turbulence through measurements related to the interstellar

magnetic field (e.g., Falceta-Gonçalves et al. 2008; Iacobelli et al. 2013; Prosekin et al. 2016; Han 2017), such as diffuse polarized synchrotron emission (e.g., Kothés et al. 2010; Wolleben et al. 2010; Mao et al. 2015), optical starlight polarization (e.g., Heiles 1996; Girart et al. 2006; Hull & Zhang 2019), Zeeman splitting (e.g., Bel & Leroy 1989; Crutcher et al. 1996; Green et al. 2012), and Faraday rotation toward background extragalactic polarized sources (e.g., Van Eck et al. 2011; Mao et al. 2012; Wu et al. 2015).

In particular, synchrotron fluctuations have great potential to provide robust statistics that can be used to give insights on the turbulence properties (e.g., Burkhart et al. 2012; Lazarian & Pogosyan 2012; Iacobelli et al. 2013). Gaensler et al. (2011) showed the advantages of using polarization gradients applied to the polarized Galactic emission to trace spatial patterns. Using a comparison with simulations, they demonstrated that turbulence in the warm-ionized medium has a relatively low sonic Mach number ( $M_S < 2$ ). Similar quantities and studies were presented to trace information from the magneto-ionic turbulent medium, such as generalized polarization gradient, polarization directional derivative, polarization directional curvature, and polarization wavelength derivative (Herron et al. 2018a, 2018b).

Techniques based on synchrotron emission also have been successfully proposed to trace magnetic field orientation. These are based on the theoretical framework proposed by Lazarian & Pogosyan (2016), which states that Alfvén and slow MHD turbulence wave modes cascade the energy anisotropically. Consequently, synchrotron intensity and polarized intensity present a gradient correlated with the direction of the magnetic field. Lazarian et al. (2017) numerically tested the efficiency of estimating the magnetic field direction using synchrotron intensity gradients (SIG) and synchrotron polarization gradients (SPG). Both techniques are based on the same principle of the method introduced in González-Casanova & Lazarian (2017) for the velocity centroid known as the “Velocity Gradient Technique” (VGT).

VGT is a technique that can obtain the magnetic field direction and strength in cold neutral regions, for line emission such as that of HI and CO (e.g., González-Casanova et al. 2019; Hsieh et al. 2019; Hu et al. 2019b, 2019c). Recently, González-Casanova & Lazarian (2019) showed that there is a good correspondence between the VGT results and the dust polarization (from stellar polarization), a useful result to map the magnetic field direction in the whole Galaxy. Soler et al. (2013) proposed the technique named Histogram of Relative Orientations (HRO), which from intensity gradients, explores how the statistics of the relative orientation of intensity gradients and magnetic fields change with column densities. The HRO technique is quite different from what was proposed in the VGT. The VGT explores the point-wise statistics of the magnetic field and does not depend on additional polarization measurements, but on elements of the MHD theory. Hu et al. (2019a) compared the differences and advantages of both techniques for different ISM conditions.

SIG and SPG represent a new way to obtain information about the magnetic field in the magneto-sonic turbulent medium. The new technique probes have been proven successful, providing information about the structure of the magnetic field. In particular the use of these gradients may provide magnetic field geometry and intensity without the effects of Faraday rotation. Moreover, Lazarian & Yuen (2018)

showed that considering Faraday depolarization, the 3D distribution of the magnetic field can be obtained in the emitting volume. The use of SPG for probing magnetic field directions at different distances from the observer was also investigated by Ho et al. (2019). Comparing to other techniques such as Faraday Tomography, the SPG can infer the magnetic field properties with a smaller frequency range. This is due to the fact that the gradients are not subjected to Faraday rotation (see Ho et al. 2019).

Additionally, Lazarian et al. (2018; hereafter LYH18) introduced two new methods, named top-base and circular standard deviation ( $S$ ), to measure  $M_A$  using velocity gradient angle distribution. In the same work, those authors made a prediction that both methods could be used to estimate the magnetization level considering the SIG and SPG contexts.

In this paper, we analyze the two proposed methods applied to synthetic synchrotron emission maps obtained from numerical simulations of ISM turbulence, in order to test their ability to retrieve the magnetization level. In Section 2 we present the theory of MHD turbulence and the connection with SIG and SPG. In Section 3, we describe the MHD simulations and in Section 4 the production of the synchrotron synthetic maps. In Section 5, we present a Bayesian approach to estimate the relevant quantities and their uncertainties. Section 6 presents the results of measuring the Alfvén Mach number using both SIG and SPG angles with different physical constraints. We further explore the effects that observing frequency, viewing angle, and signal-to-noise ratio (S/N) have on our predictive ability. Section 7 presents a discussion and the conclusions, followed by a summary of the results in Section 8.

## 2. Theoretical Considerations

Synchrotron emission is expected to occur in a magnetized plasma, which contains relativistic electrons. Though the description of turbulence for relativistic and nonrelativistic fluids requires different treatments, most of the fluids in the ISM are in the nonrelativistic regime. Assuming the mean free path of relativistic electrons in Alfvénic turbulence of Chandran (2000), Yan & Lazarian (2002, 2004), and Yan et al. (2008), one can provide a theoretical justification for the model where the synchrotron fluctuations arise from the fluctuations of magnetic fields, while the relativistic electrons are smoothly distributed in space. This picture corresponds well with the observed isotropy of the arrivals of cosmic rays with moderate energies measured at Earth (Zweibel 2013). In this context, the synchrotron emission probes the characteristics of the magnetic turbulence, which agrees with the assumptions adopted in the theory by Lazarian & Pogosyan (2012), which we rely upon in our modeling.

The modern theory of strong nonrelativistic MHD turbulence arises from Goldreich & Sridhar (1995). This turbulent model is based on anisotropic fluctuation scaling, associated with a mean magnetic field. Subsequently, (Lazarian & Vishniac 1999, henceforth LV99) extended this work, showing that magnetic reconnection does not present an impediment for the motions of a magnetic fluid that mixes the fluid in the direction perpendicular to the *local* direction of the magnetic field. In this picture, the anisotropic turbulent eddies trace the local direction of magnetic flux tubes and consequently, measurements of velocity or/and magnetic field gradients should reveal the magnetic field direction. The perpendicular turbulent mixing results in the scale-dependent anisotropy of MHD turbulence

and makes the essential distinction between MHD and hydrodynamic turbulence.

For sub-Alfvénic turbulence, the magnetic field is weakly perturbed in a range between the turbulence injection scale,  $L$ , and the transition scale  $l_{\text{trans}} = LM_A^2$ . Above this regime, the fast turbulent reconnection enhances the mixing of the eddies in the direction perpendicular to the local magnetic field. LV99 provided the eddy mixing theory description of MHD turbulence. The energy transfer (dissipative or cascade) via eddies mixing has a correspondence with the size of the eddies. The relationship between the aforementioned eddy scales follows

$$l_{\parallel} \approx L \left( \frac{l_{\perp}}{L} \right)^{2/3} M_A^{-4/3}, \quad (1)$$

where  $l_{\parallel}$  and  $l_{\perp}$  are the parallel and perpendicular eddy scales relative to the local magnetic field;  $M_A = v_L/v_A$  is the Alfvén Mach number, with  $v_L$  being the injection velocity, and  $v_A = B/\sqrt{4\pi\rho}$ , the Alfvén speed (more details can be seen in LV99). Notice that Equation (1) is similar to that formulated for the trans-Alfvénic ( $M_A = 1$ ) regime in Goldreich & Sridhar (1995), with a new dependence on  $M_A$ .

From Equation (1), one can infer that the anisotropy ratio of the eddies increases as the scales decrease. Therefore, simulations to investigate MHD anisotropies should be done at the smallest scales possible (as is the case of this work). We also have that the velocity gradient  $v_l/l_{\perp}$  increases as the scales decrease:

$$v_l/l_{\perp} \approx \left( \frac{V_A M_A^{4/3}}{L^{1/3}} \right) l_{\perp}^{-2/3}. \quad (2)$$

In the super-Alfvénic regime, the magnetic field is weak. Consequently, the kinetic energy dominates and therefore the energy cascade follows closely the Kolmogorov description up to a scale

$$l_A = LM_A^3. \quad (3)$$

Above the scale  $l_A$ , the magnetic field modifies the dynamics of the medium and the turbulence scaling can be described the same way as proposed by Goldreich & Sridhar (1995), where the anisotropy of the velocity field becomes similar to that of the sub-Alfvénic regime. In other words, the turbulence is hydrodynamic and the velocity gradients are weakly correlated with the magnetic fields. For scales smaller than  $l_A$ , the anisotropic perturbations align with the local magnetic field. Therefore, the intrinsic properties of the eddies imprinted by both regimes of Alfvénic turbulence imply not only the condition of a preferential direction along the local magnetic field, but also that the eddy velocity depends on the size of the eddies. The elongated eddies have the largest velocity gradient perpendicular to their longest axis. Thus we expect the direction of the maximum velocity gradient to be perpendicular to the local magnetic field.

The use of velocity gradient techniques to estimate the local magnetic field morphology was introduced by González-Casanova & Lazarian (2017) using numerical simulations and comparisons with other well-known techniques. In that work, the authors used velocity channel gradients to validate the new way to infer the magnetic field properties. Subsequent analysis showed that velocity gradients can also be obtained by other diagnostics such as the velocity centroid maps (VCG) and

velocity channel maps (VChG). Within the VCG context, the calculation of gradients is performed using 2D spectroscopy maps of velocity centroids, while for the VChG technique the calculation of the gradients uses the intensities within the channel maps. Both VCGs and VChGs are readily available from the Doppler-shifted spectroscopic data. There is also an additional possibility named the intensity gradient (IG) technique, which is based on the intensity from both gas and dust emission. We note that the IG technique should be distinguished from the Histograms of Relative Orientation (HRO) technique, proposed by Soler et al. (2013), which requires polarimetry data to define the direction of the magnetic fields. The IG technique is a polarization-independent method and is a way of finding the magnetic field direction, using the sub-block averaging method. This gradient technique is more affected by shocks, providing information from regions in such a condition. However, the IG technique has the limitation of being a less reliable tracer of the magnetic fields in supersonic turbulent conditions.

Lazarian & Pogosyan (2016) predicted that synchrotron emission gradients can also imprint turbulence signatures traceable by velocity gradients (locally aligned with the magnetic field). They showed that synchrotron fluctuations are also sensitive to compressible turbulence. This work opened the venues to study the synchrotron emission from our Galaxy and beyond. Regarding synchrotron fluctuations, Lazarian et al. (2017) and Lazarian & Yuen (2018) numerically confirmed that SIG and SPG can also be used to infer the magnetic field properties. Combining measurements of polarization with the SIG provides several ways to obtain synergy from the two measurements and increase the reliability of magnetic field tracing.

Since SIG are not subjected to Faraday rotation, they do not require multiple frequency measurements to compensate for the effect. One additional advantage is that measuring intensity is easier than measuring polarization. Moreover, Lazarian et al. (2018) showed that SPG and multifrequency Faraday tomography can be used to trace the 3D magnetic field structure. It is always important to have different observational techniques to study astrophysical magnetic fields since the interstellar medium presents distinct physical and chemical conditions. For instance, HI line emission from cold and warm diffuse medium, or CO emission from molecular clouds are natural environments for studies using the VCG and VChG techniques. Combining those with IG measurements, one can study shocks and self-gravitating regions (Yuen & Lazarian 2017; Hu et al. 2019a). Hence, the combined use of different molecular species to infer velocity gradients allows the study of magnetic fields and gravitational collapse within molecular clouds. Besides, both synchrotron gradients can be used not only to obtain the information on warm and hot ISM phases, but also on the 3D large-scale magnetic field distribution in galaxies. Of course, this depends on the scale over which the gradients are measured (see Appendix D in Lazarian et al. 2018 for more details).

### 3. MHD Simulations

The MHD simulations are isothermal, scale-free, compressible data cubes with a Cartesian uniform grid and  $792^3$  cells. Also, the simulations neglect self-gravity. The ZEUS-MP/HK is a well-tested code designed for astrophysical fluid dynamics simulations. The same code has been used in previous works



**Table 1**  
Simulation Parameters

$M_S$	$M_A$	$\beta = 2M_A^2/2M_S^2$	$b/B$	Description
7.31	0.22	0.002	0.15	Sub-Alfvénic
6.10	0.42	0.01	0.36	Sub-Alfvénic
6.47	0.61	0.02	0.47	Sub-Alfvénic
6.14	0.82	0.04	0.63	Trans-Alfvénic
6.03	1.01	0.06	0.76	Trans-Alfvénic
6.08	1.19	0.08	0.87	Trans-Alfvénic
6.24	1.38	0.10	1.02	Super-Alfvénic
5.94	1.55	0.14	1.12	Super-Alfvénic
5.80	1.67	0.17	1.25	Super-Alfvénic
6.55	1.71	0.19	1.39	Super-Alfvénic

(e.g., Lazarian et al. 2017, 2018; Hu et al. 2019a). These simulations are based on a simple staggered-grid finite-difference scheme (Norman 2000). The code solves the MHD equations with turbulence driving:

$$\frac{\partial \rho}{\partial t} + \nabla \cdot (\rho \mathbf{v}) = 0, \quad (4)$$

$$\frac{\partial}{\partial t}(\rho \mathbf{v}) + \nabla \cdot \left[ \rho \mathbf{v} \mathbf{v} - \frac{1}{\mu_0} \mathbf{B} \mathbf{B} - I \left( p + \frac{1}{2} \frac{B^2}{\mu_0} \right) \right] = \mathbf{f}_{\text{turb}}, \quad (5)$$

$$\frac{\partial \mathbf{B}}{\partial t} = \nabla \times (\mathbf{v} \times \mathbf{B}), \quad (6)$$

where  $\rho$  is the density,  $\mathbf{v}$  is the velocity,  $p$  is the pressure,  $\mathbf{B}$  is the magnetic field, and  $\mathbf{f}_{\text{turb}}$  is the turbulence driving force. In addition, the Characteristics Constrained Transport Method (MOCCT) was applied to guarantee divergence-free magnetic fields ( $\nabla \cdot \mathbf{B} = 0$ ) (Hayes et al. 2006).

The magnetic field consists of a mean uniform term and a fluctuating part:  $\mathbf{B} = \mathbf{B}_{\text{ext}} + \mathbf{b}$ . We initially set  $\mathbf{b} = 0$  and  $\mathbf{B}_{\text{ext}}$  along the  $x$  direction. The mean magnetic amplitude of the fluctuating part is variable and provides a range of  $\beta = 2M_A^2/M_S^2$ , where  $M_S = \langle \delta v \rangle / c_S$  is the Sonic Mach number. The values of  $\beta$ ,  $M_S$ , and  $M_A$  for each simulation are presented in Table 1. The turbulent driving scale,  $L$ , is solenoidal in Fourier space, minimizing the influence of the forcing on the generation of density structures. This scale defines the injection scale in our synthetic data. The density fluctuations are generated naturally along the runs by the interaction of MHD waves.

To simulate synthetic observations of synchrotron emission one must convert the simulation data into real units. In this work, we assume a typical box length scale  $L_{\text{box}} = 1$  kpc. The turbulent injection scale is constant and set to 0.25 kpc ( $k = 4$ ). The scale factor for the mean gas density is  $n \sim 0.03 \text{ cm}^{-3}$ , and the magnetic field  $B_{\text{ext}}$  along the  $x$  direction of strength 1.3  $\mu\text{G}$ . We also assume that the thermal electron number density,  $n_e$ , is proportional to  $n$ . An initial simulation was run with  $n_e \sim 0.01 \text{ cm}^{-3}$ . To investigate the case in which Faraday rotation is important, a simulation with  $n_e = 0.03 \text{ cm}^{-3}$  ( $\sim 100\%$  ionization fraction) was run. We expect stronger Faraday depolarization in this case and this is discussed in Section 6.3.

Here it is important to clarify that the statistics of density fluctuations in MHD turbulence is basically related to the sonic Mach number  $M_S$ . The modeling of shocks reveals that supersonic motions lead to compression that, in the isothermal approximation, result in the  $\delta\rho/\langle\rho\rangle \sim M_S^2$  relation. This is the

main cause for the broad log-normal PDF of density fluctuations in isothermal turbulence (see Passot & Vázquez-Semadeni 1998; Kowal et al. 2007).

On the other hand,  $M_A$  is linked to the dispersion and decorrelation length of  $\mathbf{B}$  fluctuations. Larger  $M_A$  result in shorter decorrelation lengths (i.e., larger power at short wavelength fluctuations) and larger amplitudes of perturbations compared to the mean field. Small values of  $M_A$ , on the contrary, are related to large decorrelation lengths and small amplitudes of  $\delta\mathbf{B}/\langle\mathbf{B}\rangle$ .

For this reason, in order to avoid combined effects of density fluctuations in the statistics of polarization vectors, we made use of models with similar  $M_S$ , and consequently, a similar PDF of density fluctuations in the models. We therefore do not expect statistically important changes in the distribution of  $\rho$ —and consequently of  $n_e$ —along the line of sight (LOS) for the different models compared. We expect changes in the statistics of Faraday depolarization only caused by different regimes of  $\delta\mathbf{B}/\langle\mathbf{B}\rangle$ . As shown below, we may characterize the models into two groups: sub-Alfvénic ( $M_A < 1$ ) and super-Alfvénic ( $M_A > 1$ ). More details on the choice of the simulation parameters can be seen in Kowal et al. (2009) and Zhang et al. (2016).

It is important to notice that the ratio between random and uniform components ( $b/B$ ), which is related to the Alfvén Mach number, is more relevant to the techniques tested in this work than the absolute amplitude of the constant field itself. The ratio of turbulent to regular field strength values can be found in Table 1. It is worth mentioning that the constant field strength in our simulations is smaller than the typical values found in the ISM ( $\sim 10\text{--}20 \mu\text{G}$ ). However, stronger turbulent fields would correspond—if the uniform component is constant—to larger  $M_A$ , possibly extrapolating the validity range of the super-Alfvénic cases studied.

#### 4. Synthetic Synchrotron Emission Maps

In order to create synthetic observations from the data cubes, we first calculate the emission and orientation of the magnetic field locally for each cell. Then we perform an integration along the LOS to produce a 2D image. We assume an isotropic pitch angle distribution and a power-law energy distribution of the electron population characterized by:

$$n_{\text{CRE}}(E)dE = n_{\text{CRE}}E^{2\gamma-1}dE, \quad (7)$$

where  $n_{\text{CRE}}(E)$  is defined as the number density of relativistic electrons with energies in the range between  $E$  and  $E + dE$ . The spectral index ( $\gamma = 2$ ) was chosen following Lazarian & Pogosyan (2012) in order to allow the comparison of our results with theirs. In addition, since all parameters in Equation (7) are constant throughout the simulation volume, the results obtained in this work are relatively insensitive to  $n_{\text{CRE}}(E)$  and  $\gamma$  fluctuations.

We also consider a source region where both synchrotron emission and Faraday rotation act simultaneously. Hence, we initially estimated the synchrotron intensity as (see Waelkens et al. 2009):

$$I(\mathbf{X}) \propto \int_0^{L_z} n_{\text{CRE}} B_{\perp}^{\gamma}(\mathbf{X}, z) dz, \quad (8)$$

where  $L_z$  is the distance between the source region and observer,  $\mathbf{X} = (x, y)$  is the two-dimensional position vector in

the plane of the sky,  $I(X)$  is the synchrotron intensity and  $B_{\perp} = \sqrt{B_x^2 + B_y^2}$  is the magnitude of the perpendicular component of the magnetic field projected on the sky.

We have to take into account that the synchrotron emission observed in the ISM is partially linearly polarized (Rybicki & Lightman 1979), being susceptible to a birefringent effect known as Faraday rotation (e.g., Haverkorn et al. 2004; Heiles & Haverkorn 2012; Zhang et al. 2016). This magneto-optical effect causes the plane of polarization to rotate as radiation propagates along the plasma.

The polarized intensity,  $P(X, \lambda^2)$ , at a given wavelength  $\lambda$  can be expressed as:

$$P(X, \lambda^2) = \int_0^{L_z} P(X, z) e^{2i\lambda^2\phi(X, z)} dz, \quad (9)$$

where  $P(X, z)$  is the intrinsic polarized intensity of the source. The associated intrinsic polarization angle is  $\theta_0(X, z)$ , and

$$\phi(X, z) = \theta_0(X, z) + \lambda^2\Phi(X, z), \quad (10)$$

and  $\phi(X, z)$  is the observed angle, with

$$\theta_0(X, z) = \frac{\pi}{2} + \tan^{-1}\left(\frac{B_y}{B_x}\right). \quad (11)$$

The Faraday depth,  $\Phi(X, z)$ , can be expressed as:

$$\Phi(X, z) = 0.81 \int_0^z n_e(X, z') B_z(X, z') dz', \quad (12)$$

where  $n_e$  is the number density of thermal electrons (in  $\text{cm}^{-3}$ ) and  $B_z$  is the LOS component of magnetic field (in  $\mu\text{G}$ ), with the distances measured in parsecs.

Using Equation (9) and considering that the final polarization is a complex vector ( $P = Q + iU$ ), the Stokes parameters  $Q$  and  $U$  can be obtained for the synchrotron emission with and without the presence of Faraday rotation. The expressions for  $Q$  and  $U$  for both cases can be found in Waelkens et al. (2009) and Lee et al. (2016), and are the same used in this work.

The final polarization,  $P$ , after integration of the Stokes parameters along the LOS, is:

$$P = \sqrt{Q^2 + U^2}, \quad (13)$$

with the angle of polarization ( $\psi$ ):

$$\psi = \frac{1}{2} \arctan\left(\frac{U}{Q}\right). \quad (14)$$

Equations (8) and (14) are used to calculate SIG and SPG. In order to obtain the intensity gradients and their angular orientations, we follow the procedure described in Yuen & Lazarian (2017), Lazarian et al. (2017), and Lazarian & Yuen (2018). Since for each pixel in the projected images there are only eight immediate neighbor pixels, the angular dependence of the gradients would be too crude, and to improve the angular resolution we first convolved the maps with 2D Gaussian kernel with a spatial  $\sigma = 2$  pixels, and then fitted this image with a 2D cubic spline. This allows interpolation on a finer grid (10 times finer in our procedure). Now the gradients can be calculated in a circle of 10 (new) cells in radius. The choice of this radius is not critical; actually it is a trade-off between small values (which degrade angular resolution, as said before) and not missing the small scales where the gradients are the best tracers of the magnetic field. The procedure was successfully

tested by Yuen & Lazarian (2017). We examined the cases of synchrotron emission alone and also the case in which Faraday rotation is included. Figure 1 shows the SIG and SPG maps in the case of synchrotron emission and Faraday rotation in the frequency range of 100, 1, and 0.1 GHz.

## 5. Error Analysis

To analyze the relationship between two variables, one can assume a probabilistic view of the problem in which a variable  $Y$  depends strictly on an observable  $X$ , as follows:

$$Y = \beta X + \epsilon, \quad (15)$$

where  $\beta$  corresponds to the parameters of the model—in this case a linear one—and  $\epsilon$  to the errors (which are assumed to be normally distributed). To find the best predictive model one can use the least squares or a maximum likelihood approach to obtain  $\beta$  and  $\epsilon$ . However, the same problem can be analyzed on a Bayesian framework, with advantages. In this approach, the model is seen as a probability distribution:

$$Y = \mathcal{N}(\beta X, \sigma^2), \quad (16)$$

where  $Y$  is a random variable that is normally distributed, with its mean being the linear predictor ( $\beta X$ ) and with a variance of  $\sigma^2$ .  $\beta$  and  $\sigma$  correspond to distributions themselves given by:

$$\beta = \mathcal{N}(\mu_{\beta}, \sigma_{\beta}^2) \quad (17)$$

$$\sigma = |\mathcal{N}(\mu_{\sigma}, \sigma_{\sigma}^2)|. \quad (18)$$

Both Equations (17) and (18) are known as priors and they quantify the initial guesses in our linear model, each characterized by a mean and standard deviation. Because all the variables correspond to probability distributions, at the end of the fitting process one can learn about the probability distributions of the parameters that give the best fit to the data (posterior distributions). The fitting process uses a Markov Chain Monte Carlo (MCMC) procedure that takes into account the information contents of the priors to obtain  $Y$ . The Bayesian analysis allows us to quantify any previous knowledge on our variables (priors) and to quantify the errors of the analysis (from the width of the posterior).

The independent variable is the Alfvén Mach number that is directly obtained from the MHD simulations, while the dependent variable is the top-base ratio, T/B, circular variance,  $V$ , or circular standard deviation,  $S$ . We first check, using the Bayesian information criterion, if a power law is the simplest model to describe the relationship between the two quantities. We use a single power law for the top-base method and two for the variance and standard deviation; one power law for each Alfvénic regime. The power laws are fitted as a linear model, and the assumed distribution and parameters for all priors are:

$$Y = \mathcal{N}(\beta M_A, \sigma^2), \quad (19)$$

$$\beta = \mathcal{N}(-1, 1), \quad (20)$$

$$\sigma = |\text{Cauchy}(0.1, 2)|. \quad (21)$$

All the results (Section 6) from the analysis done with a Bayesian approach use `Pymc3` (Salvatier et al. 2016). `Pymc3` runs an MCMC sampling to obtain the dependent variables and correspondent posterior distributions. For all fits we used 20,000 samples for each chain with 16 chains in parallel; the number of iterations to tune-up is 2000. With the parameters selected, we got a  $\hat{R}$  of 1 (up to six decimal places and at least

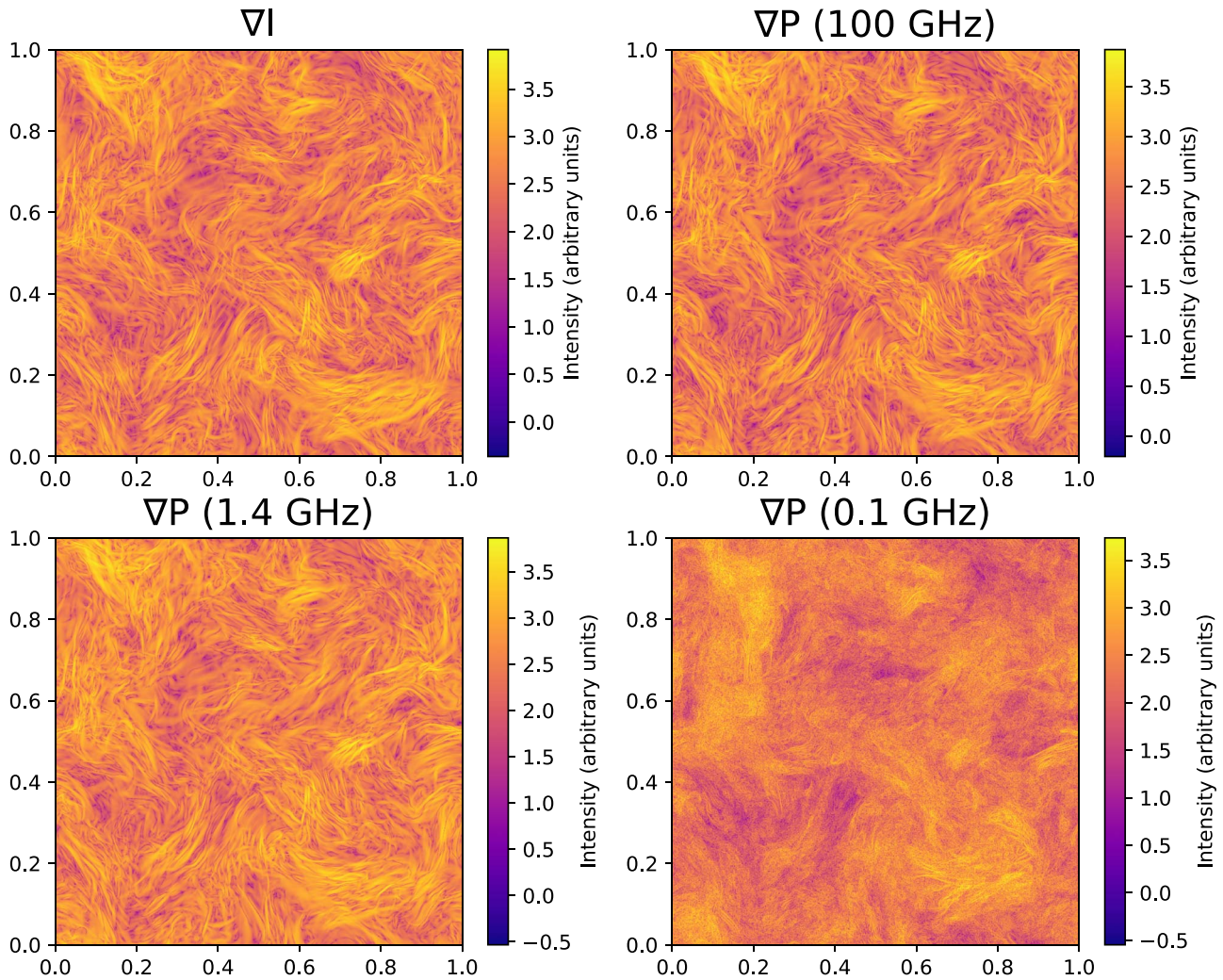


**Figure 1.** SIG (top row, left panel) and SPG images for a subsonic simulation with  $M_A = 0.8$  (see Table 1) projected along the LOS. The SPG images were produced considering Faraday rotation with a frequency of 100 GHz (top row, right panel), 1 GHz and 0.1 GHz (bottom panels). The  $x$ - and  $y$ -scales are expressed in kiloparsecs.

four depending on the specific case). Here,  $\hat{R}$  is the potential scale reduction. It evaluates if each of the chains has reached convergence.

## 6. Results

From the simulated synchrotron emission we estimate both gradients, SIG and SPG. To estimate the magnetization level as a function of the Alfvén Mach number, we use the two methods presented in LYH18, based on the synchrotron gradients (the top-base and the standard deviation methods).

For the top-base method, the angle distribution of gradients is fitted with a Gaussian profile superimposed on a constant baseline (see Figure 2), in the form:

$$F(\theta) = A \exp[-\alpha(\theta - \theta_0)^2] + B, \quad (22)$$

where  $A$  is the amplitude,  $\alpha$  controls the angle spread, and  $\theta$  is the SPG and SIG angles, with  $\theta_0$  being the location.  $B$  is the baseline of the histogram of angles. Notice that  $\psi$ , presented in Section 4, and  $\theta$  presented in this section are measured with the same coordinate system convention. Also, we emphasize that  $\theta_0$  is the location of the Gaussians fitted to distribution angles

of SPG and SIG, having a different meaning from  $\theta_0$  used in Equation (10).

The top-base method measures the ratio between the Gaussian peak and the baseline:

$$T/B = \left( \frac{A + B}{B} \right). \quad (23)$$

As seen in Figure 2, both SPG and SIG present well marked peaks for  $M_A \leq 1$ , while for  $M_A > 1$  the peak is less pronounced. As  $M_A$  increases, the top-base ratio decreases as the gradients gradually lose correlation with the magnetic field. A similar behavior happens to velocity gradients and velocity channel gradients in the context of the VGT, as presented in LYH18.

An additional approach uses the angle spread, similar to the Chandrasekhar & Fermi (1953) method. Since the angles have a  $2\pi$  periodicity, we use circular statistics instead of linear statistics. The circular variance is defined as:

$$V = 1 - R, \quad (24)$$



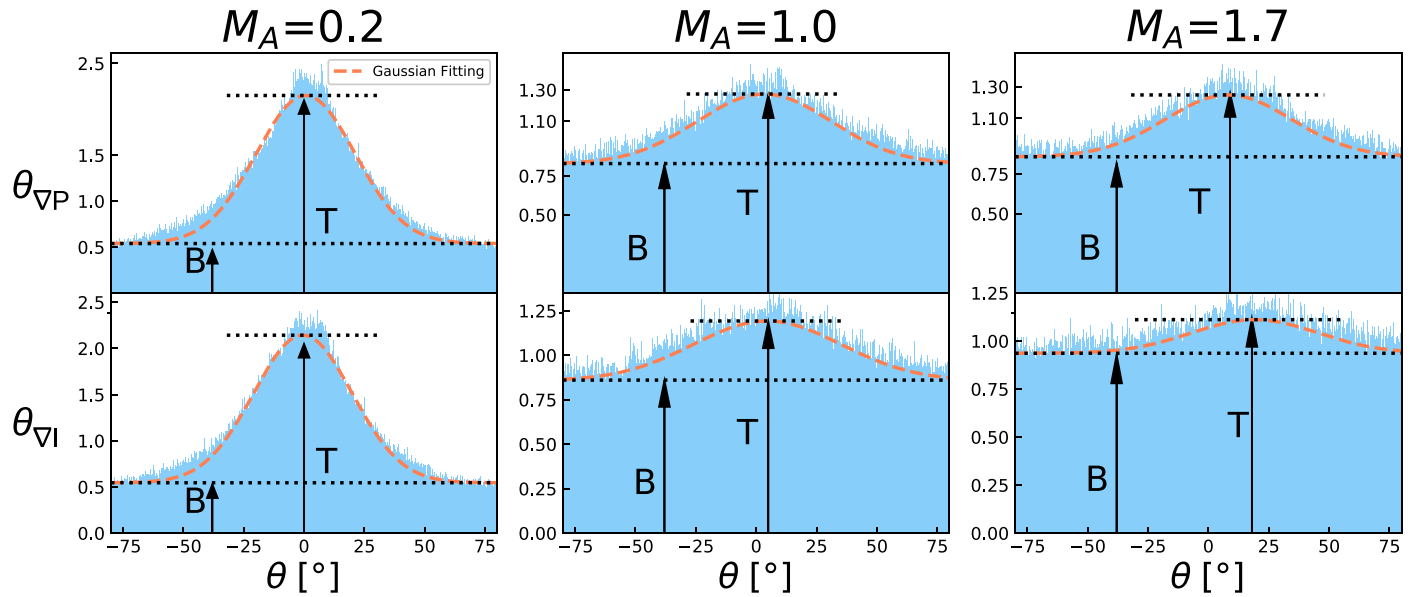


**Figure 2.** The histograms of angle distributions for synchrotron polarization gradients ( $\theta_{\nabla P}$ , top panels) and synchrotron intensity gradients ( $\theta_{\nabla I}$ , bottom panels) for three different Alfvén Mach numbers. The gradients were estimated after a Gaussian smoothing kernel was applied to the data. The red dashed line corresponds to a Gaussian fit that allows us to estimate the top (T) and the base (B) that are used to estimate the magnetic field in the top-base method.

where  $R$  is the mean resultant length defined as:

$$R = \frac{1}{N} \left\{ \left( \sum_i^N \cos(2\theta_i) \right)^2 + \left( \sum_i^N \sin(2\theta_i) \right)^2 \right\}, \quad (25)$$

and  $\theta_i$  is the angle of either SPG or SIG for each cell with  $N$  as the total number of data points. These angle gradients are calculated with the same coordinate convention as for  $\psi$ . The circular standard deviation is defined as:

$$S = \frac{1}{2} \{-2 \ln(R)\}^{1/2}. \quad (26)$$

The factor of 2 in Equation (25) is related to the fact that synchrotron gradients are calculated in the interval  $0^\circ$  and  $180^\circ$ .

Unlike in linear statistics, the variance is bound for the interval  $[0, 1]$  (Fisher 1995).  $V = 1$  means a flat distribution and  $V = 0$  is the case if all angles are coaligned. On the other hand,  $S$  is measured in the interval  $[0, \infty)$ , having properties similar to the linear standard deviation. Furthermore, because the standard deviation is not constrained, it is more susceptible to fluctuations, in particular in the super-Alfvénic regime.

Figure 3 shows the dependence of T/B,  $V$ , and  $S$  with  $M_A$  for both SIG and SPG angle distributions. The well-defined power-law relationships (Table 2) can be used to directly estimate the magnetization level from the gradients. As seen, both the top-base and the standard deviation methods work well for both gradients in the full range of magnetization probed.

The synchrotron gradients have similar trends to the velocity gradients, as estimated by LYH18. However, as seen in Figure 3, the power laws estimated for  $V$ , under super-Alfvénic regimes ( $M_A > 1$ ), present a less sensitive dependency, which makes it difficult to distinguish different levels of magnetization. For that reason, for the rest of this paper, we will exclusively use  $S$  to infer the magnetization level.

**Table 2**  
Power-law Relationships for the Three Different Methods

Method		$\nabla P$	$\nabla I$
T/B		$1.60^{+0.01}_{-0.02} M_A^{-0.54^{+0.02}_{-0.01}}$	$1.40^{+0.03}_{-0.02} M_A^{-0.64^{+0.01}_{-0.01}}$
$V$	Sub-Alfvénic	$0.90^{+0.04}_{-0.04} M_A^{0.20^{+0.08}_{-0.09}}$	$0.93^{+0.05}_{-0.07} M_A^{0.23^{+0.07}_{-0.08}}$
	Super-Alfvénic	$0.95^{+0.03}_{-0.03} M_A^{0.04^{+0.02}_{-0.02}}$	$0.89^{+0.02}_{-0.02} M_A^{0.12^{+0.03}_{-0.02}}$
$S$	Sub-Alfvénic	$1.04^{+0.03}_{-0.03} M_A^{0.24^{+0.05}_{-0.04}}$	$1.05^{+0.04}_{-0.03} M_A^{0.28^{+0.04}_{-0.04}}$
	Super-Alfvénic	$1.05^{+0.03}_{-0.02} M_A^{0.31^{+0.05}_{-0.05}}$	$1.02^{+0.03}_{-0.01} M_A^{0.26^{+0.06}_{-0.03}}$

**Note.** The linear fitting uses a Bayesian approach to estimate the parameters and uncertainties.

### 6.1. Signal-to-noise Considerations

Real observations have intrinsic noise. In order to have some perception of the effects of noise on both T/B and  $S$  presented in Figure 3, we added zero-mean Gaussian white noise to the synthetic maps on a pixel by pixel basis. This is trivially done for  $I$ . If the noise has standard deviation  $\sigma_N$  and the total pixel map intensity is  $I$ ,  $S/N = I/\sigma_N$ . However, when adding zero-mean Gaussian noise pixel by pixel to  $Q$  and  $U$ , this is tricky as the signal can be both positive and negative, and therefore the average flux over these maps can be zero. Further, in the ideal case when there is no image reconstruction related to correlated noise, the noise distribution in total intensity, and the  $Q$  and  $U$  maps will be the same. In order to provide a realistic description, we define the S/N in total intensity and compute the noise distribution for that. Then we use the same noise distribution statistics for the Stokes  $Q$  and  $U$  maps.

A 2D Gaussian kernel with a spatial  $\sigma = 2$  pixels is used to smooth the maps for the evaluation of SIG and SPG. The results are presented for  $S/N = [2, 5, 10, 15, 50, 100]$  in the total intensity map.

The SIG and SPG power laws as functions of  $M_A$  in the presence of noise can be obtained by the same procedure described before, using a Bayesian analysis approach that

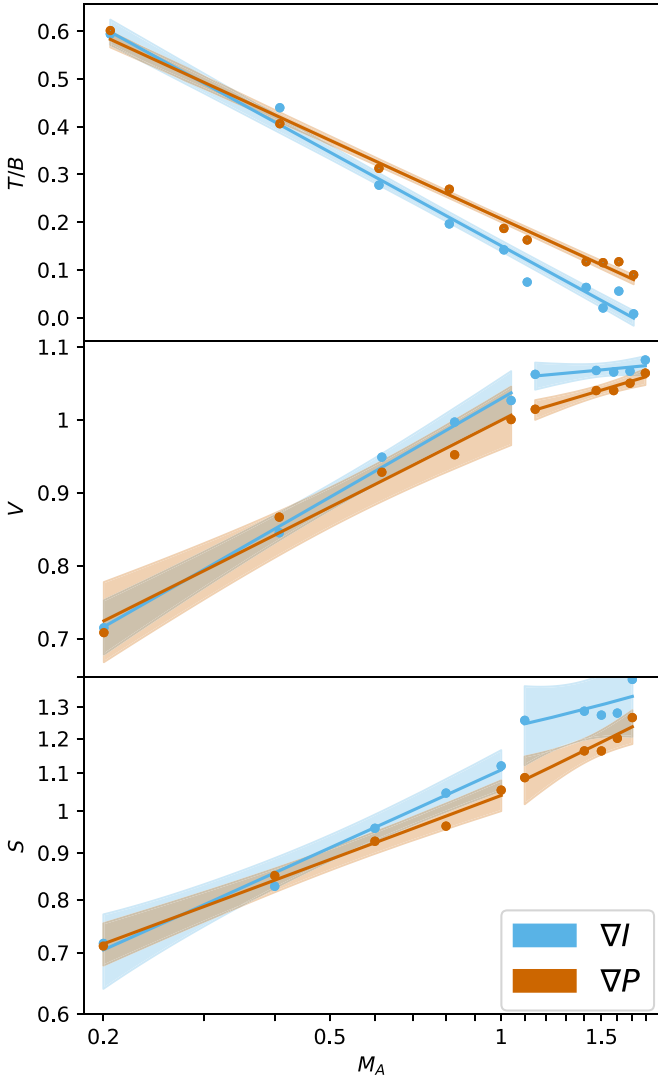


**Figure 3.** The relationships between the top-base ratio (T/B, top panel), the circular variance ( $V$ , middle panel) and the circular standard deviation ( $S$ , bottom panel) with respect to the Alfvén Mach number for both SIG (cyan) and SPG (brown). The regions  $M_A < 1$  (sub-Alfvénic) and  $M_A > 1$  (super-Alfvénic) are treated separately for  $V$  and  $S$ . The trend lines are estimated using a Bayesian approach, that allows realistic uncertainty estimates, in this case  $1\sigma$ , for both SIG and SPG. The relevant parameters of the power-law fits can be found in Table 2.

allows a fair estimate of uncertainties. We obtained both gradients for 10 values of  $M_A$  and six different S/N ratios. We applied the procedure for the top-base ratio and the circular standard deviation methods. Figure 4 shows the effects of the S/N on the synchrotron gradients considering the SIG case. We found the same behavior for the SPG case.

For the circular standard deviation method, it is clear that for  $S/N \gtrsim 5$  the method behaves well and one can properly derive the Alfvén Mach number (for the sub-Alfvénic regimes). For the super-Alfvénic regime a single value of  $S$  can correspond to multiple values of the Mach number, if one includes the  $1\sigma$  errors, therefore one can only give an upper limit to the magnetic field strength. The relationship between  $S$  and  $M_A$  with  $1\sigma$  errors for SIG is:

$$M_A = \begin{cases} 0.84^{+0.11}_{-0.09} S_I^{3.6^{+0.3}_{-0.3}}, & \text{if } M_A < 1. \\ 0.93^{+0.10}_{-0.04} S_I^{3.8^{+0.7}_{-0.5}}, & \text{if } M_A \geq 1, \end{cases} \quad (27)$$

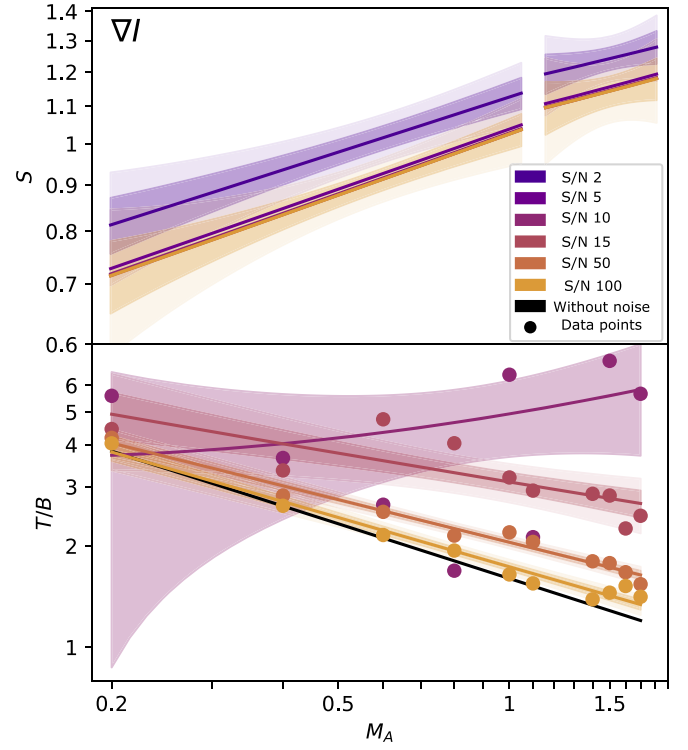


**Figure 4.** Power-law fits of the circular standard deviation ( $S$ , top panel) and top-base ratio (T/B, bottom panel) as functions of the Alfvén Mach number for the SIG. The different colors correspond to different S/N ratios, with a case without noise (only possible in computer simulations) added. The regions  $M_A < 1$  (sub-Alfvénic) and  $M_A > 1$  (super-Alfvénic) are treated separately. In the top panel, only the uncertainties ( $1\sigma$  and  $2\sigma$ ) for the trend lines of S/N = 2 and S/N = 100 are shown, for better visualization. The power-law fits and uncertainties are estimated with a Bayesian approach. The SPG (not shown) has a similar behavior as the SIG with respect to the effects of noise levels.

and for SPG:

$$M_A = \begin{cases} 0.85^{+0.09}_{-0.11} S_P^{4.2^{+0.7}_{-0.8}}, & \text{if } M_A < 1. \\ 0.85^{+0.07}_{-0.05} S_P^{3.2^{+0.4}_{-0.6}}, & \text{if } M_A \geq 1. \end{cases} \quad (28)$$

We see in Figure 4 that T/B versus  $M_A$  is more sensitive to the S/N ratio, and should be used only in cases of  $S/N \gtrsim 5$ .

## 6.2. Influence of the Mean Magnetic Field Direction on SIG and SPG Angle Distributions

It is important to know how the projection effects may change the results from synchrotron gradient angle dispersion techniques. The mean magnetic field  $\langle B \rangle$ , is oriented parallel to the  $x$ -axis and varies with respect to the LOS with an angle  $\alpha$  (i.e., rotates around the  $y$ -axis). The LOS and the mean magnetic field are perpendicular for  $\alpha = 0^\circ$ , and parallel for  $\alpha = 90^\circ$ . Considering different values of  $\alpha$ , the 3D data cubes produce the following projected quantities:  $B_x = \langle B \rangle \cos \alpha$  and  $B_z = \langle B \rangle \sin \alpha$ . Thus, approaching  $90^\circ$  gives the largest ( $\sin 90^\circ = 1$ ) mean field contribution to the Faraday depth. A consistent integration path along the LOS for any  $\alpha$  is guaranteed by a periodic replication of the basic simulation cube (e.g., Falceta-Gonçalves et al. 2008; Zhang et al. 2019a).

Figure 5 shows the relationship between circular standard deviation for different angles  $\alpha$  and the Alfvén Mach number for both SIG and SPG. Note that we are now considering the



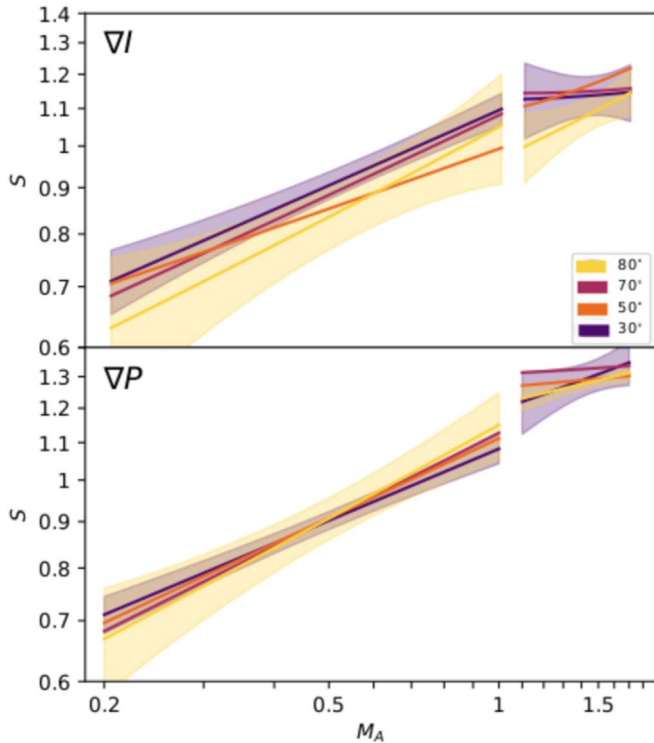


**Figure 5.** Power-law fits of the circular standard deviation,  $S$ , for SIG (top panel) and SPG (bottom panel) as a function of  $M_A$  for different angles  $\alpha$ . The trend lines are estimated using a Bayesian approach, which allows the estimation of the uncertainties in this case,  $1\sigma$ . Only the uncertainties for  $80^\circ$  (purple) and  $30^\circ$  (yellow) cases are presented. The regions  $M_A < 1$  (sub-Alfvénic) and  $M_A > 1$  (super-Alfvénic) are treated separately. Faraday rotation effects are not considered in this analysis.

combined effects of both constant and random components of the magnetic field, without Faraday rotation. We explore different angle configurations,  $\alpha = 80^\circ, 70^\circ, 50^\circ$ , and  $30^\circ$ . Figure 5 shows that decreasing angles  $\alpha$  show a slight improvement in terms of the associated uncertainties. This behavior is expected since the synchrotron gradients measure the apparent direction of the magnetic field on the plane of the sky. If the plane of the sky component of the mean magnetic field is weak, the turbulent component will become relatively more important, and the gradients are not going to provide the projected direction accurately.

### 6.3. Faraday Rotation Effects

Synchrotron emission is susceptible to Faraday rotation effects that have been disregarded so far. Our synthetic polarization maps taking into account Faraday rotation use the same data set and input physical assumptions used in Zhang et al. (2019b). The thermal electron density and magnetic field strength are set to  $n_e \sim 0.03 \text{ cm}^{-3}$  and  $B_{\parallel} \sim 1.3 \mu\text{G}$ . As shown in that work, Faraday rotation depends on frequency, as expected, and on the Alfvénic regime of the turbulence. To summarize the relevant statistics in the two different regimes, the rotation measure calculated for  $M_A = 0.2$  and  $n_e = 0.03 \text{ cm}^{-3}$  ranges from  $-2.0$  to  $12.3 \text{ rad m}^{-2}$ , with a mean value of  $7.7 \pm 0.1 \text{ rad m}^{-2}$ , while for  $M_A = 1.0$ , it ranges from  $-2$  to  $86 \text{ rad m}^{-2}$  and the mean value is  $20 \pm 1 \text{ rad m}^{-2}$ .

A compact way of visualizing the effects of the progressively larger Faraday rotation for lower and lower frequencies is the use of the alignment measure (AM), which describes the

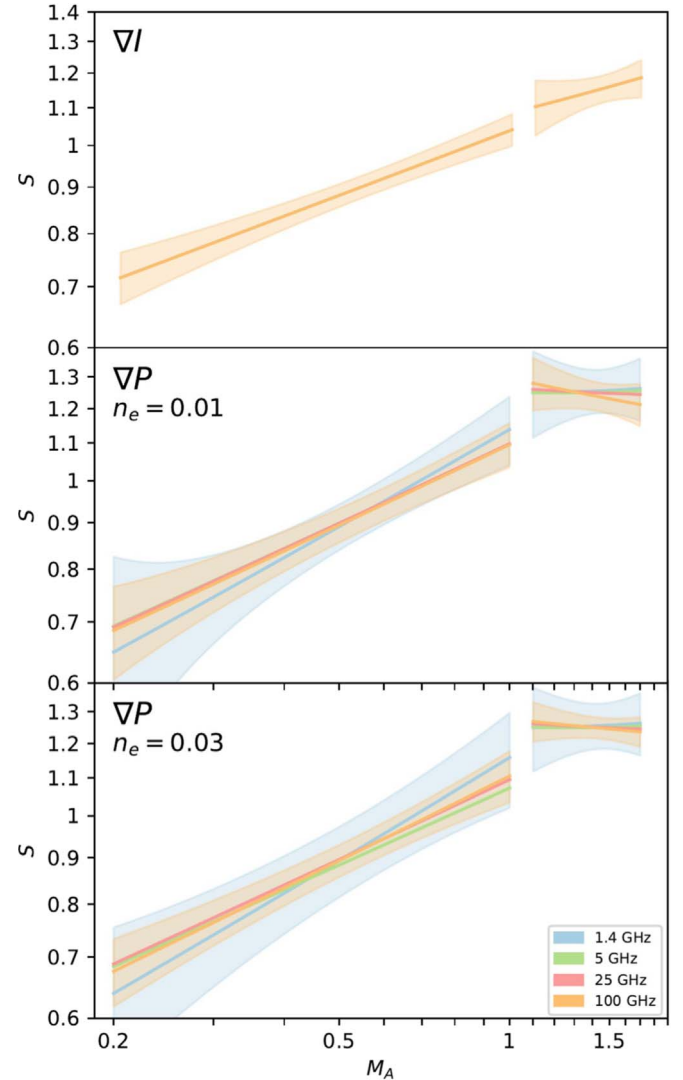


**Figure 6.** Power-law fits of the circular standard deviation,  $S$ , for SIG (top panel) and SPG (lower panels) as a function of  $M_A$ . The regions  $M_A < 1$  (sub-Alfvénic) and  $M_A > 1$  (super-Alfvénic) are treated separately. The different colors correspond to different frequencies to show the effects of Faraday rotation. The trend lines are estimated using a Bayesian approach, that allows realistic uncertainty estimates. In this case,  $1\sigma$  errors are shown for the 1.4 GHz and 100 GHz frequencies, which are extreme cases. The lower panels show cases for two different electronic densities.

correspondence between SIG, SPG, and the polarization vector quantity (see González-Casanova & Lazarian 2017). The definition of AM is

$$\text{AM} = 2\langle \cos^2 \phi \rangle - 1. \quad (29)$$

AM is analogous to the Rayleigh reduction factor in the dust alignment theory suggested by Greenberg et al. (1968).  $\phi$  is the angle between the measured magnetic field direction and the intrinsic magnetic field. When  $\text{AM} = -1$ , the magnetic field is perpendicular to SPG or SIG. When  $\text{AM} = 1$ , they have a perfect alignment, whereas random orientations result in  $\text{AM} \sim 0$ . Lazarian et al. (2017) showed that AM for the magnetic field and SIG is in the range of 0.78–0.95 at 1 GHz.

Figure 6 shows the relationship between the circular standard deviation ( $S$ ) and the Alfvén Mach number for different frequencies. It is clear that regardless of the frequency, SIG can

measure very well the magnetization level, especially in the sub-Alfvénic regime where the correlation is more pronounced. Also, there is no dependence of the result with the mean density of the medium. The reason for this is the fact that the intensity map is insensitive to Faraday rotation, and its consequent depolarization. Also, being an intensity normalized function,  $S$  calculated for SIG is also insensitive to varying  $n_e$ .

This is not the case for the polarization maps, and consequently for the SPG statistics. Synchrotron polarization suffers Faraday depolarization along the LOS, and depends on the observational wavelength and the density of the medium. For this reason, to check these effects, we have calculated the  $S$  parameter of SPG for two different values of density, namely  $n_e = 0.01$  and  $0.03 \text{ cm}^{-3}$ , and frequencies between 1.4 and 100 GHz. We found that in the sub-Alfvénic regime, lower frequencies tend to show a larger correlation between  $S$  and  $M_A$ . However, as can be seen in Figure 6, all lines shown lie within the  $1\sigma$  uncertainty region from each other, with no significant change in slope in a range of  $\sim 2$  orders of magnitude in frequency. A factor of 3 in mean density also does not result in significant change in the slope or the absolute value of  $S$ .<sup>6</sup> For the super-Alfvénic regime, it is still possible to use a linear trend to model the magnetization level with SIG but the power-law description breaks up for the SPG case. Given these uncertainties, only upper limits to the magnetic field strength would be obtained from SPG in the super-Alfvénic regime.

Overall, it is evident that the SIG and SPG angle distributions can measure the magnetization level, considering the range of parameters probed in this work. Future work may explore and extend this analysis to higher magnetic field values and consequently higher values of Faraday rotation effects, in order to check its validity for other regimes.

## 7. Discussion and Conclusions

A synergistic analysis combining MHD simulations, statistical analysis, and observational data provides a potential way to characterize the interstellar turbulence and magnetic field distributions. The works of Zhang et al. (2019a, 2019b) and Hu et al. (2019a, 2019b) used such a combination to study polarization and velocity gradients (from line emission) aiming to explore the different properties of the ISM. Here we explore MHD simulations to validate the T/B,  $V$ , and  $S$  diagnostics for the orientation of synchrotron gradients in the presence of Faraday rotation with weak depolarization effects, considering both sub- and super-Alfvénic regimes.

Regarding the effects of the S/N ratio in the results, in Section 6.1 we showed that for values  $S/N < 10$ , the top-base method presents limitations. Fortunately, the circular standard deviation method is still well correlated with  $M_A$ , even for lower values of the S/N ratio. Since meaningful measurements of synchrotron emission at radio wavelengths have a threshold around  $S/N = 5$ , the application of the standard deviation method is viable even at this limit. In order to have a fair assessment of the accuracy of the results, we used a Bayesian approach, together with an MCMC sampling scheme for investigating the relations between  $M_A$  and the relevant indicators in Section 5.

<sup>6</sup> Note that we plot  $S$  versus  $M_A$ , which is dependent on  $n^{1/2}$ . Therefore, for the same  $S$  value, the magnetic field intensity estimated from the bottom panel of Figure 6 will be  $\sqrt{3}$  larger than its value obtained from middle panel.

We addressed the effects of the orientation of the mean magnetic field with respect to the LOS, and checked whether it can limit the applicability of the technique. As shown in Section 6.2, the statistics of the gradients, as a proxy to estimate  $M_A$ , is preserved for a broad range of angles.

Following LYH18 and Zhang et al. (2019a) who tested the effect of the alignment of the synchrotron gradients with the local magnetic field when the emission is subject to Faraday depolarization, in our work, we also considered the influence of weak Faraday depolarization regimes in order to test if the techniques explored here can still be applied to estimate the magnetization level. For both low and high frequencies, the SPG angles are weakly affected by Faraday rotation. The results indicate that the circular statistics analysis is valid for regimes where the conventional polarization vector approach does not behave well. Our results indicate that  $M_A$  may be recovered using the  $S$  diagnostic, which works well in the presence of weak depolarization effects. In a future work, we intend to explore the applicability of this technique when stronger depolarization polarization effects and higher value magnetic fields are present. This is important since it is closer to the typical observational values of the mean and turbulent magnetic fields in the ISM, and would be suitable for analyzing the high resolution ISM data collected by the last generation of radio-telescopes, as the Low Frequency Array (LOFAR), the Australian Square Kilometre Array Pathfinder (ASKAP), and the Square Kilometre Array (SKA). This would be complemented by the higher frequencies coverage and smaller field-of-view instruments like the Atacama Large Millimeter Array (ALMA) and the Very Large Array (VLA), meaning that the combination of these resources can provide the magnetization levels for small and large scales of the ISM.

The results reported here do not take into account the influence of synchrotron self-absorption along the LOS, telescope beam smoothing effects, and variations in the distribution of relativistic electrons.

## 8. Summary

In this work, we numerically tested the validity of the methodology introduced by LYH18, to estimate the magnetization level of the ISM based on velocity centroid gradients, but now making use of the angle distributions of SPGs and SIGs. We provided calculations for ranges of parameters that correspond to some regions of the ISM of observational interest, though not covering the full range of parameters found in the Galactic diffuse interstellar medium. The main results are summarized as follows:


1. We found that in order to estimate the magnetization level based on observations, the dependence on S/N is more severe for the top-base method, but still reliable with the standard deviation method close to  $S/N \sim 5$ .
2. Choosing the circular standard deviation method as the most promising, we applied the technique for different orientations of the LOS with respect to the mean magnetic field. We were able to recover the magnetization levels for angles  $\alpha \gtrsim 30^\circ$ .
3. We studied the effect of Faraday rotation in simulations with  $n_e = 0.01 \text{ cm}^{-3}$  and  $0.03 \text{ cm}^{-3}$  and found that the circular variance statistics can still be used to estimate the magnetization level at different wavelengths, when weak depolarization effects are considered.

4. There is a good correlation between  $M_A$  and both SIG and SPG for the sub-Alfvénic regime. We were able to recover the magnetization level for the whole range of parameters examined.

We thank Julie Davis, Zach Pace, Ka Ho Yuen, Hue Yue, Junda Chen, Aysses do Carmo, Cintia Schwantes, Eunice Jesus, and Victor Lazarian for the insightful discussions. L.C. acknowledges financial and travel support by Brazilian agency CAPES-Finance code 001. D.F.G. thanks the Brazilian agencies CNPq (#311128/2017-3) and FAPESP (#2013/10559-5) for financial support. D.F.G.C. and A.L. acknowledges support by NSF AST 1816234. D.F.G.C. was partially supported by CONACyT (Mexico). M.C. thanks FAPESP (#2015/25972-0). J.F.Z. thanks the supports from the National Natural Science Foundation of China (grant No. 11703020). I.S.F. passed away during the final stage of the writing of this paper. We express our condolences to the family.

### ORCID iDs

Lorena Carmo  <https://orcid.org/0000-0002-0096-3048>

Diego F. González-Casanova  <https://orcid.org/0000-0002-4827-0558>

Diego Falceta-Gonçalves  <https://orcid.org/0000-0002-1914-6654>

### References

- Armstrong, J. W., Rickett, B. J., & Spangler, S. R. 1995, *ApJ*, **443**, 209
- Baker, P. L. 1973, *A&A*, **23**, 81
- Ballesteros-Paredes, J., Klessen, R. S., Mac Low, M. M., & Vázquez-Semadeni, E. 2007, in *Protostars and Planets V*, ed. B. Reipurth, D. Jewitt, & K. Keil (Tucson, AZ: Univ. Arizona Press), 63
- Bel, N., & Leroy, B. 1989, *A&A*, **224**, 206
- Beresnyak, A., & Lazarian, A. 2019, *Turbulence in Magnetohydrodynamics* (Berlin: De Gruyter)
- Brandenburg, A., & Lazarian, A. 2013, *SSRv*, **178**, 163
- Brandenburg, A., Sokoloff, D., & Subramanian, K. 2012, *SSRv*, **169**, 123
- Burkhart, B., Falceta-Gonçalves, D., Kowal, G., & Lazarian, A. 2009, *ApJ*, **693**, 250
- Burkhart, B., & Lazarian, A. 2011, in *ASP Conf. Ser. 444, Statistical Tools of Interstellar Turbulence: Bridging the Gap Between Numerics and Observations*, ed. N. V. Pogorelov, E. Audit, & G. P. Zank (San Francisco, CA: ASP), 9
- Burkhart, B., Lazarian, A., & Gaensler, B. M. 2012, *ApJ*, **749**, 145
- Chandran, B. D. G. 2000, *PhRvL*, **85**, 4656
- Chandrasekhar, S., & Fermi, E. 1953, *ApJ*, **118**, 113
- Chepurnov, A., Burkhart, B., Lazarian, A., & Stanimirovic, S. 2015, *ApJ*, **810**, 33
- Chepurnov, A., Gordon, J., Lazarian, A., & Stanimirovic, S. 2008, *ApJ*, **688**, 1021
- Chepurnov, A., & Lazarian, A. 2010, *ApJ*, **710**, 853
- Correia, C., Lazarian, A., Burkhart, B., Pogosyan, D., & De Medeiros, J. R. 2016, *ApJ*, **818**, 118
- Crutcher, R. M., Roberts, D. A., Mehringer, D. M., & Troland, T. H. 1996, *ApJL*, **462**, L79
- Elmegreen, B. G., & Scalo, J. 2004, *ARA&A*, **42**, 211
- Ensor, T., Cami, J., Bhatt, N. H., & Soddu, A. 2017, *ApJ*, **836**, 162
- Esquivel, A., Lazarian, A., Pogosyan, D., & Cho, J. 2003, *MNRAS*, **342**, 325
- Falceta-Gonçalves, D., Kowal, G., Falgarone, E., & Chian, A. C.-L. 2014, *NPGeo*, **21**, 587
- Falceta-Gonçalves, D., Lazarian, A., & Kowal, G. 2008, *ApJ*, **679**, 537
- Falgarone, E., Hily-Blant, P., & Pineau Des. Forêts, G. 2005, in *ESA Special Publication 577, Proc. Dusty and Molecular Universe: A Prelude to Herschel and ALMA*, ed. A. Wilson (Noordwijk: ESA), 75
- Federrath, C., Klessen, R. S., & Schmidt, W. 2008, *ApJL*, **688**, L79
- Fisher, N. I. 1995, *Statistical Analysis of Circular Data* (Cambridge: Cambridge Univ. Press)
- Gaensler, B. M., Haverkorn, M., Burkhart, B., et al. 2011, *Natur*, **478**, 214
- Girart, J. M., Rao, R., & Marrone, D. P. 2006, *Sci*, **313**, 812
- Goldreich, P., & Sridhar, S. 1995, *ApJ*, **438**, 763
- González-Casanova, D. F., & Lazarian, A. 2017, *ApJ*, **835**, 41
- González-Casanova, D. F., & Lazarian, A. 2019, *ApJ*, **874**, 25
- González-Casanova, D. F., Lazarian, A., & Burkhart, B. 2019, *MNRAS*, **483**, 1287
- González-Casanova, D. F., Lazarian, A., & Cho, J. 2018, *MNRAS*, **475**, 3324
- Green, J. A., McClure-Griffiths, N. M., Caswell, J. L., Robishaw, T., & Harvey-Smith, L. 2012, *MNRAS*, **425**, 2530
- Greenberg, J. M., Middlehurst, B. M., & Aller, L. H. 1968, in *Nebulae and Interstellar Matter*, ed. B. M. Middlehurst & L. H. Aller (Chicago, IL: Univ. Chicago Press), 221
- Han, J. L. 2017, *ARA&A*, **55**, 111
- Haverkorn, M., Brown, J., Gaensler, B., & McClure-Griffiths, N. 2008, *ApJ*, **680**, 362
- Haverkorn, M., Katgert, P., & de Bruyn, A. G. 2004, *A&A*, **427**, 549
- Hayes, J. C., Norman, M. L., Fiedler, R. A., et al. 2006, *ApJS*, **165**, 188
- Heiles, C. 1996, *ApJ*, **462**, 316
- Heiles, C., & Haverkorn, M. 2012, *SSRv*, **166**, 293
- Herron, C. A., Burkhart, B., Gaensler, B. M., et al. 2018a, *ApJ*, **855**, 29
- Herron, C. A., Gaensler, B. M., Lewis, G. F., & McClure-Griffiths, N. M. 2018b, *ApJ*, **853**, 9
- Heyer, M., Gong, H., Ostriker, E., & Brunt, C. 2008, *ApJ*, **680**, 420
- Heyer, M. H., & Peter Schloerb, F. 1997, *ApJ*, **475**, 173
- Hily-Blant, P., & Falgarone, E. 2009, *A&A*, **500**, L29
- Ho, K. W., Yuen, K. H., Leung, P. K., & Lazarian, A. 2019, *ApJ*, **887**, 258
- Hsieh, C.-h., Hu, Y., Lai, S.-P., et al. 2019, *ApJ*, **873**, 16
- Hu, Y., Yuen, K. H., & Lazarian, A. 2019a, *ApJ*, **886**, 17
- Hu, Y., Yuen, K. H., Lazarian, A., et al. 2019b, *ApJ*, **884**, 137
- Hu, Y., Yuen, K. H., Lazarian, V., et al. 2019c, *NatAs*, **3**, 776
- Hull, C. L. H., & Zhang, Q. 2019, *FrASS*, **6**, 3
- Iacobelli, M., Haverkorn, M., Orrú, E., et al. 2013, *A&A*, **558**, A72
- Kothes, R., Landecker, T. L., & Willis, A. G. 2010, in *ASP Conf. Ser. 438, The Dynamic Interstellar Medium: A Celebration of the Canadian Galactic Plane Survey*, ed. R. Kothes et al. (San Francisco, CA: ASP), 111
- Kowal, G., Lazarian, A., & Beresnyak, A. 2007, *ApJ*, **658**, 423
- Kowal, G., Lazarian, A., Vishniac, E. T., & Otmianowska-Mazur, K. 2009, *ApJ*, **700**, 63
- Krumholz, M. R., & Burkhart, B. 2016, *MNRAS*, **458**, 1671
- Lazarian, A. 2005, in *AIP Conf. Ser. 784, Magnetic Fields in the Universe: From Laboratory and Stars to Primordial Structures*, ed. E. M. de Gouveia dal Pino, G. Lugones, & A. Lazarian (Melville, NY: AIP), 42
- Lazarian, A., & Pogosyan, D. 2004, *ApJ*, **616**, 943
- Lazarian, A., & Pogosyan, D. 2006, *ApJ*, **652**, 1348
- Lazarian, A., & Pogosyan, D. 2012, *ApJ*, **747**, 5
- Lazarian, A., & Pogosyan, D. 2016, *ApJ*, **818**, 178
- Lazarian, A., & Vishniac, E. T. 1999, *ApJ*, **517**, 700
- Lazarian, A., & Yuen, K. H. 2018, *ApJ*, **865**, 59
- Lazarian, A., Yuen, K. H., Ho, K. W., et al. 2018, *ApJ*, **865**, 46
- Lazarian, A., Yuen, K. H., Lee, H., & Cho, J. 2017, *ApJ*, **842**, 30
- Lee, H., Lazarian, A., & Cho, J. 2016, *ApJ*, **831**, 77
- Makarenko, I., Fletcher, A., & Shukurov, A. 2015, *MNRAS*, **447**, L55
- Makarenko, I., Shukurov, A., Henderon, R., et al. 2018, *MNRAS*, **475**, 1843
- Mao, S. A., McClure-Griffiths, N. M., Gaensler, B. M., et al. 2012, *ApJ*, **755**, 21
- Mao, S. A., Zweibel, E., Fletcher, A., Ott, J., & Tabatabaei, F. 2015, *ApJ*, **800**, 92
- McKee, C. F., & Ostriker, E. C. 2007, *ARA&A*, **45**, 565
- Norman, M. L. 2000, *RMxAC*, **9**, 66
- O'Dell, C. R., & Castaneda, H. O. 1987, *ApJ*, **317**, 686
- Oey, M. S., & Clarke, C. J. 1997, *MNRAS*, **289**, 570
- Ossenkopf, V., Krieps, M., & Stutzki, J. 2008, *A&A*, **485**, 917
- Ostriker, E. C. 2003, in *Turbulence and Magnetic Fields in Astrophysics*, ed. E. Falgarone & T. Passot (Berlin: Springer), 252
- Passot, T., & Vázquez-Semadeni, E. 1998, *PhRv*, **58**, 4501
- Planck Collaboration, Adam, R., Ade, P. A. R., & Aghanim 2016, *A&A*, **594**, A1
- Prosekin, A. Y., Kelner, S. R., & Aharonian, F. A. 2016, *PhRvD*, **94**, 063010
- Rybicki, G. B., & Lightman, A. P. 1979, *Radiative Processes in Astrophysics* (New York: Wiley)
- Salvatier, J., Wiecki, T. V., & Fonnesbeck, C. 2016, *PeerJ Computer Science*, **2**, e55
- Scheffler, H. 1967, *ZA*, **65**, 60
- Soler, J. D., Hennebelle, P., Martin, P. G., et al. 2013, *ApJ*, **774**, 128
- Stanimirovic, S., Staveley-Smith, L., van der Hulst, J. M., et al. 2000, *MNRAS*, **315**, 719



- Stutzki, J., Bensch, F., Heithausen, A., Ossenkopf, V., & Zielinsky, M. 1998, *A&A*, **336**, 697
- Van Eck, C. L., Brown, J. C., Stil, J. M., et al. 2011, *ApJ*, **728**, 97
- von Weizsäcker, C. F. 1951, *ApJ*, **114**, 165
- Waelkens, A. H., Schekochihin, A. A., & Enßlin, T. A. 2009, *MNRAS*, **398**, 1970
- Wolleben, M., Fletcher, A., Landecker, T. L., et al. 2010, *ApJL*, **724**, L48
- Wu, Q., Kim, J., & Ryu, D. 2015, *NewA*, **34**, 21
- Yan, H., & Lazarian, A. 2002, *PhRvL*, **89**, 281102
- Yan, H., & Lazarian, A. 2004, *ApJ*, **614**, 757
- Yan, H., Lazarian, A., & Petrosian, V. 2008, *ApJ*, **684**, 1461
- Yuen, K. H., & Lazarian, A. 2017, *ApJL*, **837**, L24
- Zhang, J.-F., Lazarian, A., Ho, K. W., et al. 2019a, *MNRAS*, **486**, 4813
- Zhang, J.-F., Lazarian, A., Lee, H., & Cho, J. 2016, *ApJ*, **825**, 154
- Zhang, J.-F., Liu, Q., & Lazarian, A. 2019b, *ApJ*, **886**, 63
- Zweibel, E. G. 2013, *PhPI*, **20**, 055501
- Zweibel, E. G., & Heiles, C. 1997, *Natur*, **385**, 131